# Growth of Metal–Metal Oxide Nanostructures on Freestanding Graphene Paper for Flexible Biosensors

*Fei Xiao, Yuanqing Li, Xiaoli Zan, Kin Liao, Rong Xu, and Hongwei Duan**

**Flexible biosensors are of considerable current interest for the development of portable point-of-care medical products, minimally invasive implantable devices, and compact diagnostic platforms. A new type of flexible electrochemical sensor fabricated by depositing high-density Pt nanoparticles on freestanding reduced graphene oxide paper (rGOP) carrying $MnO_2$ nanowire networks is reported. The triple-component design offers new possibilities to integrate the mechanical and electrical properties of rGOP, the large surface area of $MnO_2$ networks, and the catalytic activity of well-dispersed and small-sized Pt nanoparticles prepared via ultrasonic-electrodeposition. The sensitivity and selectivity that the flexible electrode demonstrates for nonenzymatic detection of $H_2O_2$ enables its use for monitoring $H_2O_2$ secretion by live cells. The strategy of structurally integrating metal, metal oxide, and graphene paper will provide new insight into the design of flexible electrodes for a wide range of applications in biosensing, bioelectronics, and lab-on-a-chip devices.**

## 1. Introduction

Flexible biosensors that can accommodate dramatic shape changes are instrumental for the development of portable point-of-care medical products, minimally invasive implantable devices, and compact diagnostic platforms.[1–4] Biosensors based on electrochemical readout represent a major class of analytical tools in clinical applications.[5] As the primary functioning components of electrochemical sensors, carbon substrates with immobilized noble metal nanostructures typically serve as working electrodes to promote the redox reactions of analytes of interest.[6,7] Recent advances in the production of carbon and metal nanomaterials have greatly diversified the possible building blocks for the hybrid electrodes.[8] However, the performance of the hybrid electrodes relies on not only the properties of individual components, such as the electron transport ability of carbon substrates and the catalytic activities of metal nanostructures, but also the effective and scalable structural integration of the two components. Great efforts have been directed to generate stable and high-density loading of nanostructured electrocatalysts on carbon substrates by taking advantages of the functional groups on the carbon substrates or physically adsorbed organic mediators.[9–12] In addition, the design of flexible electrochemical biosensors creates special needs for freestanding carbon substrates with superior mechanical strength and flexibility.

Here, we report a triple-component flexible biosensor fabricated by sequentially growing $MnO_2$ nanowire networks and Pt nanoparticles on freestanding reduced graphene oxide (rGOP). Recent discovery of graphene has stimulated considerable research activities on the optical, electronic, and mechanical properties of this single-atom-thick 2D carbon material and its hierarchical assemblies.[13–18] The directed assembly of individual graphene nanosheets into macroscopic paper-like materials is of particular interest for the development of flexible electrode because the resultant freestanding graphene paper has shown a unique collection of characteristics, such as mechanical robustness, excellent electrical conductivity, and stability in electrochemical environment, outperforming many other carbon substrates.[19–24] As shown in **Figure 1**, graphene paper used in this study was fabricated by evaporating the aqueous dispersion of exfoliated graphene oxide (GO) nanosheets in casting molds, followed by chemical reduction. To circumvent the low-loading of metal catalysts resulting from the limited surface area of the 2D rGOP substrate, we have developed template-free electrodeposition of $MnO_2$ nanowire networks on rGOP to produce a 3D network with large surface areas. Metal oxides are actively pursued to support metal particles for heterocatalysis and electrocatalysis.[25–27] Here, the use of $MnO_2$ nanowire networks gives rise to interconnected porous 3D frameworks with abundant reactive sites and large surface areas for the deposition of nanostructured Pt. Among a large family of noble metals, metallic Pt or Pt oxides are the most catalytically active species used in electrocatalysis.[28,29] A number of wet-chemical and electrochemical approaches have been explored to synthesize Pt nanostructures with controlled sizes and morphologies. We have used ultrasonic-electrodeposition to grow Pt nanoparticles on the $MnO_2$ network coated graphene paper. Ultrasonic-electrodeposition is a modified electrochemical approach in which the use of ultrasonication during electrodeposition process results in the generation of small nanocrystals with good size distribution, providing great versatility in synthesizing nanocatalysts for catalytic or sensing processes.[30–32] Our results also demonstrate that the structural integration of the three building blocks into flexible electrodes successfully overcome the problems associated with

Dr. F. Xiao, Dr. Y. Li, X. Zan, Prof. K. Liao, Prof. R. Xu, Prof. H. Duan
School of Chemical and Biomedical Engineering
Nanyang Technological University
70 Nanyang Drive, Singapore 637457
E-mail: hduan@ntu.edu.sg

DOI: 10.1002/adfm.201200191

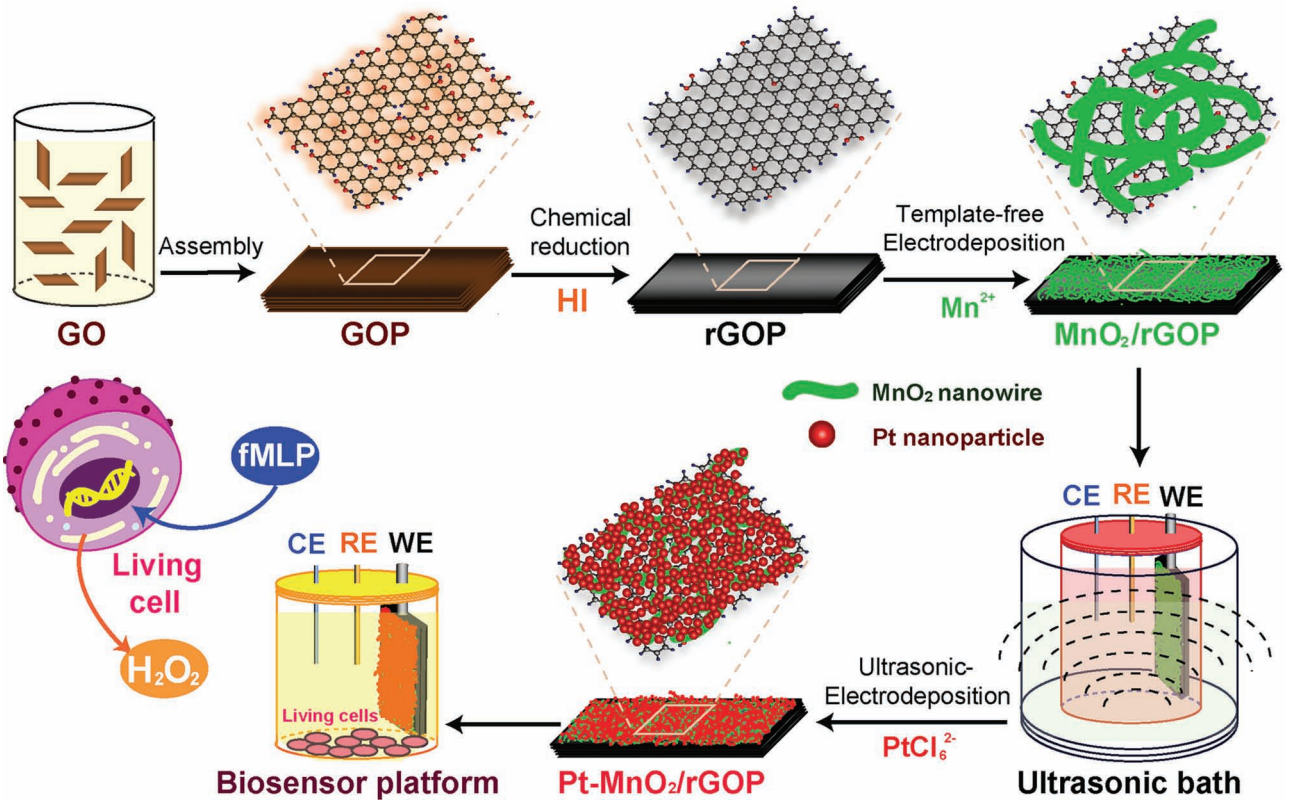


**Figure 1.** Illustrative fabrication process of the paper electrode for the biosensor platform.

two-component systems such as the low loading density of metal nanoparticles on rGOP and the low electrical conductivity and activity of semiconducting $MnO_2$. The use of rGOP carrying $MnO_2$ nanowire networks to support Pt nanoparticles leads to flexible electrodes with large active surface areas, fast electron transport, and excellent electrocatalytic activity, which is confirmed by the sensitive and selective nonenzymatic detection of $H_2O_2$. More importantly, our tertiary electrodes also exhibit fast response time, long-term stability and reproducibility, and tolerance to physical deformation, which offer possibilities for the real-time detection of $H_2O_2$ secretion by live cells. In comparison with various existing enzymatic $H_2O_2$ biosensors based on hemoglobin, horseradish peroxidase, or cytochrome c, nonenzymatic $H_2O_2$ sensors can overcome the intrinsic problems of enzymatic sensors such as poor stability of enzymes and interference from electroactive species.[33–37] Another unique advantage of our strategy is that both of the production of graphene paper through mold-casting and the electrodeposition of $MnO_2$ nanowire networks and Pt nanoparticles do not have size limits, offering great flexibility for scaling-up in practical applications.

## 2. Results and Discussion

### 2.1. Characterization of the Free-Standing Electrode

GO nanosheets were prepared by ultrasonication-assisted exfoliation of graphite oxide obtained via a modified Hummers method.[38] Atomic force microscopy (AFM) observation (see Supporting Information, Figure S1) shows that the GO nanosheets are mostly single-layered graphene with a thickness of about 1.0 nm.[21] Freestanding GO paper (GOP) was fabricated using a simple and scalable mold-casting method. Scanning electron microscopy (SEM) images (**Figure 2**A–C) reveal that GOP has a uniform thickness throughout its cross-section and GO nanosheets align in parallel to form a layer-by-layer structure. The resultant GOP was then chemically reduced using HI solution to partially restore the 2D ordered structure of graphene, which was damaged during the oxidation reaction and exfoliation. As displayed in Figure 2D–F, the layered stacking of the nanosheets and the wrinkle feature on the paper surface are maintained in rGOP. However, it is apparent that the nanosheets become more densely packed in rGOP, which should be due to the removal of a large fraction of oxygen containing groups such as hydroxyl and epoxy on GO nanosheets by chemical reduction.[39–42] Recent report by Cheng and co-workers has shown that HI reduces GO through the ring-opening reaction of epoxy groups and the substitution reaction of hydroxyl groups.[22] Notably, this evaporation-assisted assembly of GO nanosheets coupled with the post-assembly chemical reduction provides opportunities to adjust the dimension and thickness of the freestanding paper by simply choosing different sized molds or using varying volume of GO dispersion.

The growth of Pt–$MnO_2$ nanostructures on rGOP substrates was carried out in two steps. First, an interconnected network of $MnO_2$ nanowires was introduced through potentiodynamic

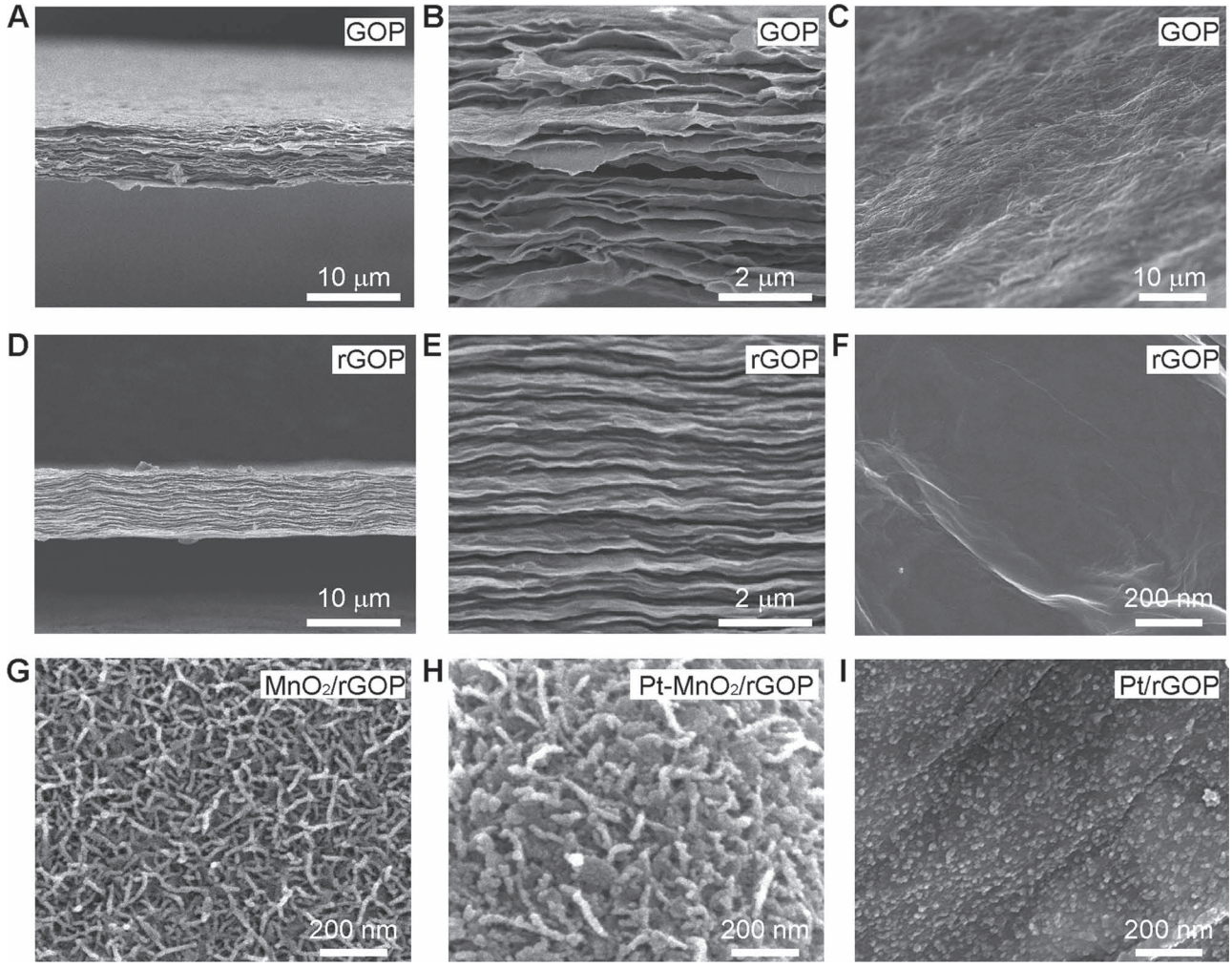


**Figure 2.** Cross-sectional and top view SEM images of different paper substrates.

electrodeposition. Second, Pt nanoparticles were grown via controlled potentiostatic ultrasonic-electrodeposition. We have developed a template-free electrodeposition protocol to achieve the complete coverage of the rGOP surface by the $MnO_2$ nanowire network (Supporting Information Figure S2). The wrinkle feature of rGOP is invisible because of the high density of $MnO_2$ nanowires on rGOP. SEM image at higher magnification (Figure 2G) shows that the $MnO_2$ nanowires have a typical diameter of ≈10 to 15 nm and an average length of ≈100 to 200 nm. The core-level X-ray photoelectron spectrum (XPS) of Mn 2p reveals the $2p_{3/2}$ and $2p_{1/2}$ peaks centered at 642.0 and 653.5 eV (Supporting Information Figure S3), confirming that $MnO_2$ is the predominant chemical constituent of the nanowire.[43] Furthermore, the amount of $MnO_2$ loaded can be readily controlled by adjusting the cycle sweep segments during the potentiodynamic electrodeposition process. Next, the controlled ultrasonic-electrodeposition of Pt nanoparticles is carried out under high-intensity ultrasonic irradiation generated from ultrasonic agitation, which causes physiochemical effects, such as enhanced mass-transport, surface cleaning, and radical formation.[27–29] All of these effects contribute to the minimized particle aggregation and therefore are helpful to deposit tiny nanoparticles on conductive substrates. Evidently, the resultant Pt nanoparticles (Figure 2H) form a shielding layer around the $MnO_2$ nanowires and also fill in the void space in the network, indicating the high affinity of the Pt nanoparticles to the $MnO_2$ frameworks. The same deposition process leads to Pt nanoparticles with lower density on bare rGOP substrates, as shown in Figure 2I. In this case, the wrinkle feature of rGOP is visible. In contrast, the Pt particles deposited on rGOP in absence of ultrasonication tend to form large clusters of small particles and inhomogeneous distribution on the substrate (Supporting Information Figure S4). Because of the significantly increased surface areas and the assistance of ultrasonication, this approach makes it possible to achieve high mass loading of Pt nanoparticles, which is expected to improve the performance of the electrode in electrocatalysis applications.

**Figure 3**A shows that the dark brown-colored GOP turned into black after reduced in HI solution and rGOP exhibits a shining metallic luster on both sides, which is a result of the improved electron transport properties after the conjugated $sp^2$-hybridized network is partially recovered.[22] The stress–strain

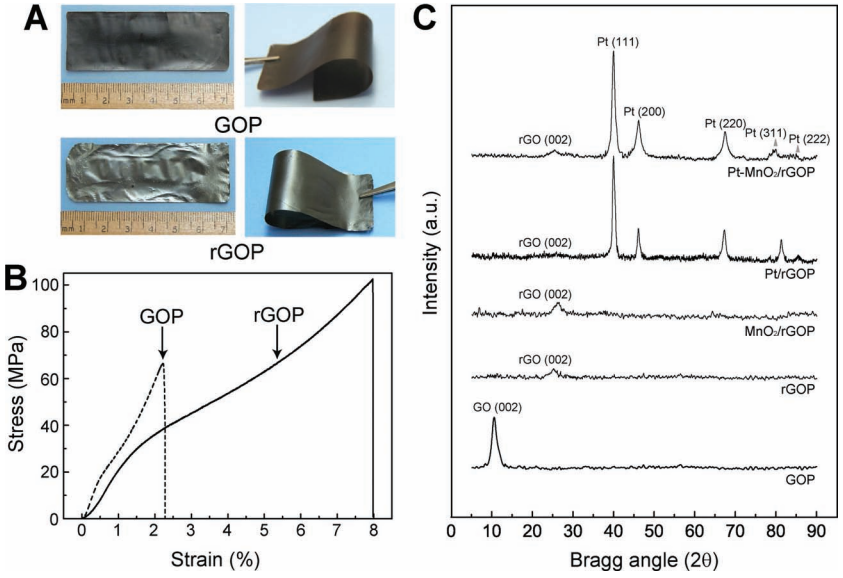


**Figure 3.** A) Optical photographs and B) stress–strain curve of the GOP and rGOP. C) XRD patterns of different papers.

curve (Figure 3B) of a typical GOP specimen reveals a straightening behavior at the beginning followed by a roughly linear (i.e., elastic) behavior. Such a trend is similar to what has been reported previously.[21–23] GOP has a tensile strength of 67.1 MPa and a ultimate tensile strain of 2.44% (Supporting Inforamtion Table S1), indicative of its acceptable strength, elasticity, and ductility. Notably, the tensile strength and strain of rGOP increase to 102.4 MPa and 8.09%, respectively. The enhanced tensile strength and ductility of rGOP should be due to the stronger interlayer interaction of rGO nanosheets following the elimination of the oxygen-containing groups on the GO nanosheets, which is in line with the densely packed layered structures observed in SEM images (Figure 2D,E).

X-ray diffraction (XRD) measurements are used to investigate the crystal structure of the three components of rGOP. As shown in Figure 3C, the XRD pattern of GOP exhibits only one peak centered at 10.4°, corresponding to the (002) reflection of stacked GO sheets with a layer-to-layer distance (*d*-spacing) of 0.85 nm. In comparison, rGOP displays a much weaker and broader diffraction peak of (002) diffraction at about 25.5° and a decreased *d*-spacing of 0.35 nm, further confirming the elimination of the oxygen-containing groups on the graphene sheets.[14,44,45] The electrodeposition of $MnO_2$ nanowires on rGOP did not lead to the appearance of new diffraction peaks other than the one arising from the rGOP substrate, indicating the low crystallinity of the $MnO_2$ nanowires. In addition to the broad peak at $2\theta = 25°$ of the rGOP substrate, the XRD patterns (Figure 3C) of Pt–$MnO_2$/rGOP and Pt/rGOP show five characteristic peaks of face centered cubic (fcc) crystalline Pt (JCPDS-ICDD, Card No. 4-802) at $2\theta$ values of about 39.9, 46.1, 67.4, 81.2, and 85.5°, which correspond to (111), (200), (220), (311), and (222) planes, respectively. This indicates that the Pt nanocatalysts have principally single-phase disordered structures. The average crystalline size of Pt nanoparticles is derived from the Debye–Scherrer equation, showing that the crystalline size (5.2 nm) of Pt nanoparticles on Pt–$MnO_2$/rGOP is smaller than that (9.6 nm) on Pt/rGOP.

Electrochemical impedance spectroscopy (EIS) provides important information about the interfacial properties of electrodes. **Figure 4**A shows the Nyquist plots of Pt–$MnO_2$/rGOP, $MnO_2$/rGOP, rGOP and GOP electrodes in the presence of equimolar of $[Fe(CN)_6]^{3-/4-}$. These Nyquist plots is fitted by an equivalent circuit (inset in Figure 4A), where the Faradic charge transfer resistance ($R_{ct}$) corresponds to the semicircle at high frequencies, solution resistance ($R_s$) is the intersection of the curve at real part $Z'$ in the high frequencies range, and the Warburg impedance ($W$) is the slope of the curves at a low frequency. Evident differences in Faradic charge transfer resistance are observed for the electrodes at different stages of modification (see Supporting Information Table S2 for details). In contrast to the large charge transfer resistance of insulating GOP, rGOP exhibits accelerated electron transfer due to the restoration of $sp^2$-hybridized network ($R_{ct}$ = 355 Ω) in rGOP.[45] Introducing semiconducting $MnO_2$ on rGOP leads to an increase of $R_{ct}$ to 420 Ω. Finally, the growth of Pt nanoparticles on $MnO_2$/rGOP substrates causes a considerable reduction in $R_{ct}$ (177 Ω), implying that the semiconducting $MnO_2$ nanowires are well-shielded by Pt nanoparticles. Figure 4B depicts cyclic voltammetry (CV) curves of Pt–$MnO_2$/rGOP and Pt/rGOP scanned in deaerated 0.1 M $H_2SO_4$ solutions within a potential range from –0.2 to 1.0 V. The hydrogen adsorption/desorption that characterize polycrystalline bulk Pt are readily seen, indicating that highly electroactive Pt nanoparticles have been effectively loaded on the two flexible substrate. The cathodic or anodic charge under the parts of CV curves in the hydrogen adsorption/desorption region are used to estimate the electrochemically active surface area of individual electrodes.[46] The active surface areas (38.6 $m^2\ g^{-1}$) of Pt–$MnO_2$/rGOP displays an over 100% increase relative to that (18.4 $m^2\ g^{-1}$) of Pt/rGOP, benefiting from the higher loading and smaller size of Pt nanoparticles on the $MnO_2$/rGOP support. Taken together, both of the enhanced electron transfer property and large active surface areas favorably indicate the enhanced electrocatalytic activities of the triple-component Pt–$MnO_2$/rGOP flexible electrode.

### 2.2. Electrochemical Sensing Performance

To evaluate the electrocatalytic activity and sensing performance of Pt–$MnO_2$/rGOP, $H_2O_2$ is chosen as a model analyte, and an electrochemical detection platform for real-time tracking the secretion of $H_2O_2$ by live cells is established in our work. $H_2O_2$, as the most stable reactive oxygen species, is an important mediator for the intracellular redox reactions and also leads to oxidative damages to cells when misregulated accumulation happens. Thus, the development of biosensors for sensitive detection of $H_2O_2$ is of considerable interest.[47–50]

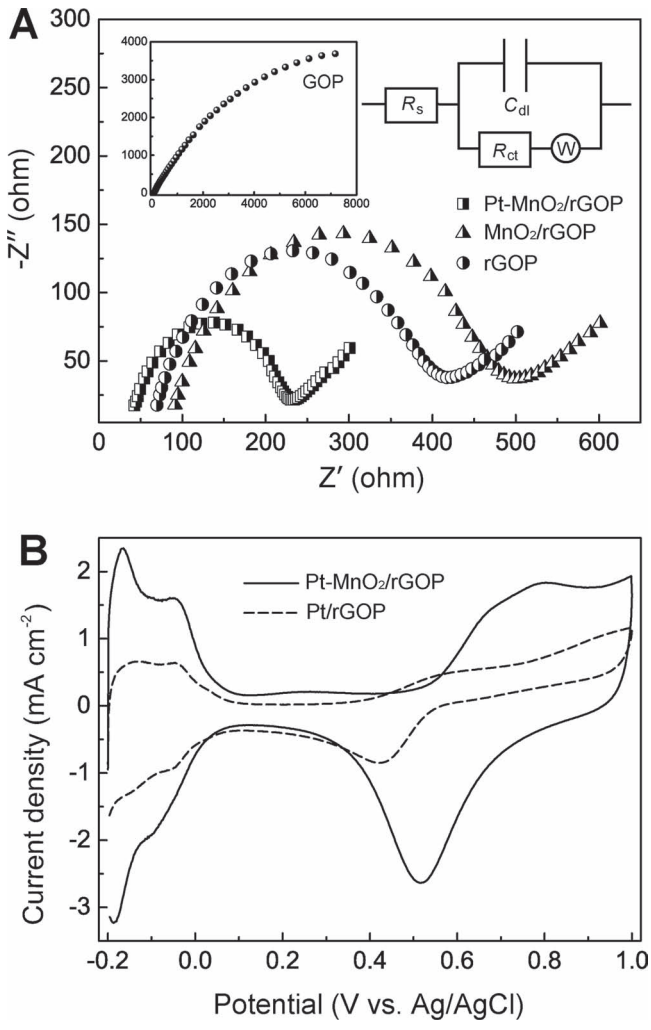


**Figure 4.** A) Nyquist plots of Pt–$MnO_2$/rGOP, $MnO_2$/rGOP and rGOP electrodes in 0.1 M KCl containing 1.0 mM $K_3Fe(CN)_6$, and 1.0 mM $K_4Fe(CN)_6$. Frequency range: 0.1 Hz to $10^5$ Hz. The inset is the Nyquist plots of GOP and the equivalent circuit. B) CV curves of Pt–$MnO_2$/rGOP and Pt/rGOP electrodes in 0.5 M $H_2SO_4$ saturated with nitrogen gas. Scan rate: 50 mV $s^{-1}$.

**Figure 5**A shows CV curves of Pt–$MnO_2$/rGOP along with control electrodes such as Pt/rGOP, $MnO_2$/rGOP, and rGOP in 0.1 M oxygen-free phosphate buffer solution (PBS) containing 5 mM $H_2O_2$. Pt–$MnO_2$/rGOP electrode exhibits a pair of well-defined oxidation/reduction peaks associated with the oxidation and reduction of $H_2O_2$. The reduction peak potential is 60 mV more positive than that of Pt/rGOP electrode and the peak current density is much larger as well, signifying that Pt–$MnO_2$/rGOP has a higher catalytic activity to the reduction of $H_2O_2$ than Pt/rGOP. In contrast, $MnO_2$/rGOP electrode gives rise to a pair of unconspicuous reduction and oxidation peaks with a larger overpotential, and no obvious oxidation and reduction peak of $H_2O_2$ was detected in the same potential range for bare GOP.

Selectivity and sensitivity are the most critical factors for sensing application, and particularly for amperometric detection, it is important to select a suitable detection potential to

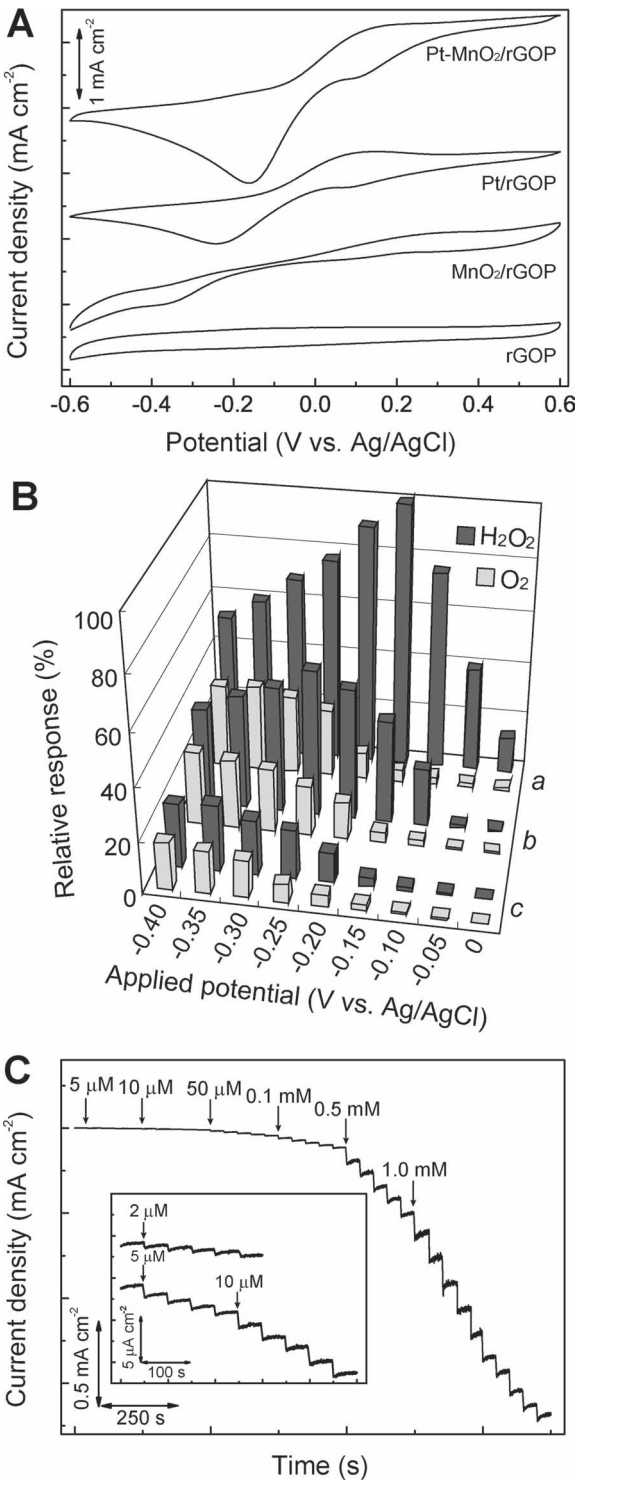


**Figure 5.** A) CV curves of Pt–$MnO_2$/rGOP, Pt/rGOP, $MnO_2$/rGOP and rGOP electrodes in 0.1 M PBS (pH 7.4) containing 5 mM $H_2O_2$. Scan rate: 50 mV $s^{-1}$. B) Dependence of amperometric responses of Pt–$MnO_2$/rGOP (a), Pt/rGOP (b), and $MnO_2$/rGOP (c) electrodes for oxygen interference. C) Typical amperometric response of Pt–$MnO_2$/rGOP electrode to successive addition of different $H_2O_2$ concentration in a stirring solution of PBS (pH 7.4). The inset is the amperometric responses of Pt–$MnO_2$/rGOP electrode at low concentrations to be detected. Applied potential: –0.15 V.

obtain highly sensitive current response and to eliminate interferences. The reduction peak of $H_2O_2$ at the Pt–$MnO_2$/rGOP electrode occurs at a relatively negative potential. Our results show that the present $H_2O_2$ biosensor operated at a selected negative detection potential (–0.15 V) is free of interference from a variety of cathodic and anodic species (Supporting Information Table S3). However, the interference from oxygen is significant because oxygen normally coexists with $H_2O_2$ in biological systems, and the oxygen reduction commonly occurs at a negative potential. Figure 5B compares the amperometric response of 1.0 mM $H_2O_2$ in PBS buffer saturated with oxygen gas at the Pt–$MnO_2$/rGOP, Pt/rGOP, and $MnO_2$/rGOP electrodes. Obviously, the interference of oxygen is large for all the electrodes at potentials below –0.25 V. With the applied detection potential shifts to positive values, the electrochemical response of oxygen decreases dramatically. At the applied detection potential of –0.15 V, the interference of oxygen becomes negligible, and the reduction current of $H_2O_2$ reaches maximum value for Pt–$MnO_2$/rGOP. Collectively, among the flexible electrode tested, Pt–$MnO_2$/rGOP yields much better sensing performance in terms of both sensitivity and selectivity.

Amperometric responses of Pt–$MnO_2$/rGOP to successive concentration changes of $H_2O_2$ were measured at the optimized potential of –0.15 V and the corresponding current-time responses are shown in Figure 5C. With aliquot additions of $H_2O_2$, well-defined steady-state cathode current responses are obtained within 3 s and the currents increase stepwise. The calibration plot of steady-state currents against the concentration of $H_2O_2$ is depicted in Figure 5C. Pt–$MnO_2$/rGOP-based senor shows a linear dynamic range of 2.0 μM to 13.33 mM (**Figure 6**A) with a sensitivity of 129.5 μA $cm^{-2}$ $mM^{-1}$ and a detection limit down to 1.0 μM (signal-to-noise ratio of 3). The stability of the Pt–$MnO_2$/rGOP electrode has been investigated by monitoring its amperometric response over a period of 1800 s in 1.0 mM $H_2O_2$ solution. The current retains 95% of its initial value (Supporting Information Figure S5), suggesting that $H_2O_2$ and its reduction products have no inhibitory effect on the electrode response. The long-term storage stability of the Pt–$MnO_2$/rGOP electrode has also been evaluated by measuring the electrode responses at intervals of one week. About 90% of their original responses (Supporting Information Figure S5) can still be detected after 48 days. The reproducibility of the biosensors is examined by successive measurements of 1.0 mM $H_2O_2$ using one sensor. Ten repeated measurements using the same electrode yield relative standard deviation (RSD) of 3.1%. Moreover, the RSD of the current responses of over 10 sensors prepared with the same method is 5.5% (Supporting Information Figure S6). These results are indicative of the high stability and accuracy of the sensor for long-term and repeated uses.

### 2.3 Flexibility Testing

Flexibility is of critical importance for the use of the paper electrode in the fabrication of miniaturized lab-on-a-chip devices and advanced implantable biomedical devices for the in vitro and in vivo analysis of real-life samples.[1,2] For this reason, the effect of the bending-induced mechanical stress on the overall sensing performance of flexible Pt–$MnO_2$/rGOP electrode has been investigated. The influence of the bending-induced mechanical stress upon the concentration-dependence for $H_2O_2$ is illustrated in Figure 6A. Over the entire $H_2O_2$ concentration range from 2.0 μM to 13.33 mM, the sensitivity of the as-prepared flexible biosensor remains constant before and after a 180° bending (Figure 6A). As shown in Figure 6B, upon bent inward to angles of 45°, 90°, and 180°, the flexible Pt–$MnO_2$/rGOP electrode exhibits minimal change in the amperometric response to 1.0 mM $H_2O_2$. The effect of the bending time and the number of repeated 180° bending are also investigated. The results show that extensive and repetitive bending has a negligible impact on the $H_2O_2$ sensing. The change of amperometric responses to 1.0 mM $H_2O_2$ is less than 5% after bending for 24 h or 100 times. These findings indicate that the electrochemical behaviors of the flexible sensor are nearly independent of the bending states, which allow it to be rolled up and incorporated into specialized system for micro-biomedical devices.

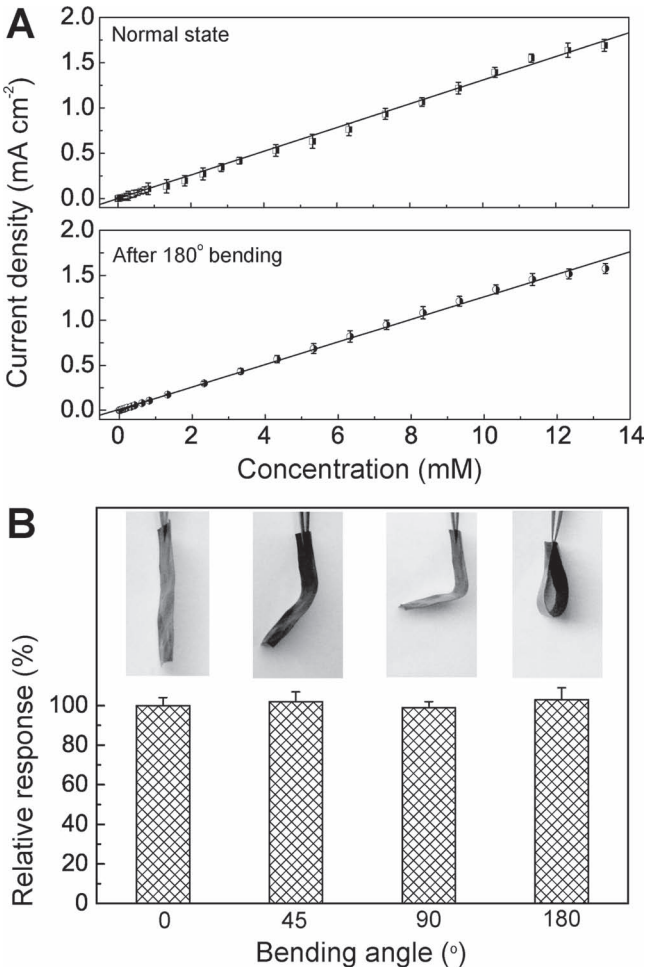


**Figure 6.** A) Effects of bending angles on the current response to 1.0 mM $H_2O_2$ using the flexible Pt–$MnO_2$/rGOP electrode. B) Calibration curves corresponding to the detection of $H_2O_2$ concentration over the full linear range (from 2.0 μM to 13.33 mM) using the flexible Pt–$MnO_2$/rGOP electrode obtained before and after a 180° bending.

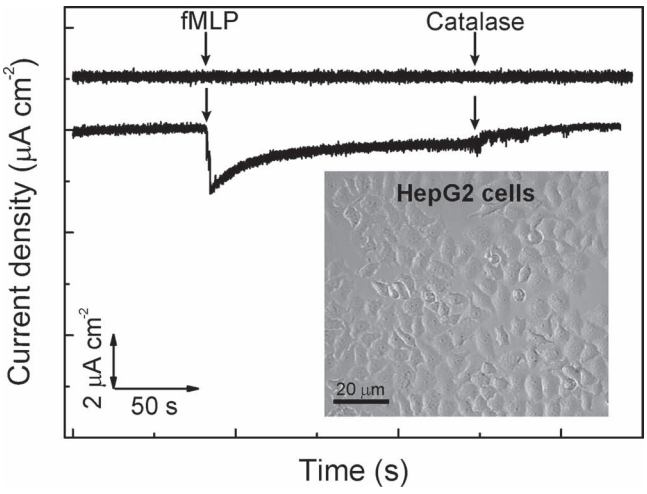


**Figure 7.** Amperometric responses of the Pt–$MnO_2$/rGOP electrode in 0.1 M PBS (pH 7.4) with the addition of 10 μM fMLP and 300 U $mL^{-1}$ catalase in the absence (upper) and present (bottom) of HepG2 cells. The inset is the bright-field microscopy image of HepG2 cells.

### 2.4. Detection of Extracellular $H_2O_2$ Released from Human Liver Cancer Cells

Encouraged by the optimal performance, i.e., the broad linear dynamic range, low detection limit, high sensitivity and selectivity, long stability, and good reproducibility, of our triple-component flexible $H_2O_2$ biosensor, we used it for real-time tracking $H_2O_2$ secretion by live cells. The cells of 80% confluency (**Figure 7** inset) are induced to release $H_2O_2$ by injecting *N*-formyl-methionyl-leucyl-phenylalanine (fMLP). Upon the addition of 10 μM fMLP, a significant increased current is observed at the Pt–$MnO_2$/rGOP electrode, followed by a gradual decrease of current, and reaches a plateau at 0.83 μA $cm^{-2}$ after 40 s. Furthermore, the addition of catalase, which is a $H_2O_2$ scavenger, results in a sudden drop of current response followed by progressive decease down to the level of background signal afterwards. Control wells containing no HepG2 liver cancercells do not generate any signal response to the addition of fMLP or catalase (Figure 7). This observation substantially demonstrates that the flexible $H_2O_2$ biosensor based on Pt–$MnO_2$/rGOP electrode establishes a sensitive, reliable, and robust method for the routine determination of $H_2O_2$ secreted by live cells and could potentially be useful for further physiological and pathological investigations.

## 3. Conclusions

In summary, we have demonstrated the preparation of a new type of flexible Pt–$MnO_2$/graphene nanohybrid paper by the sequential electrodeposition of $MnO_2$ nanowires and Pt nanoparticles on a freestanding graphene paper substrate. This Pt–$MnO_2$/graphene paper has several unique features including i) using freestanding graphene paper with excellent conductivity and mechanical properties as a robust substrate for the template-free electrodepositon of $MnO_2$ nanowires and the further fabrication of flexible hybrid electrode; ii) employing interconnected porous 3D frameworks of $MnO_2$ nanowires for enhanced loading of Pt nanocatalyst; and iii) growing catalytically active Pt nanoparticles on the freestanding support through ultrasonic electrodeposition. These integrated features allow for its use in real-time detecting $H_2O_2$ secreted by live cells. We envision that our strategy of structurally integrating of metal, metal oxide, and graphene paper into flexible electrodes will provide new insight into the design of flexible biosensors for biomedical applications, such as potable diagnostic devices and miniaturized sensors.

## 4. Experimental Section

*Chemicals and Apparatus*: Potassium hexachloroplatinate ($K_2PtCl_6{\cdot}6H_2O$, purity: 99%), manganese sulfate ($MnSO_4$, purity: 99%), graphite powder, HI (55%), and $H_2O_2$ were obtained from Aldrich. The stock solution of $H_2O_2$ was prepared by diluting 30% $H_2O_2$ solution and standardized by titration with a standard solution of potassium permanganate. The freshly prepared $H_2O_2$ stock solution was stored in an amber-glass bottle in refrigerator (4 °C) prior to the experiments. The working solutions were prepared by diluting the stock solution with PBS and water. All other chemicals used were of analytical reagent grade.

The tensile behaviors of GOP and rGOP were measured using an Instron 8848 Microforce Tester at a loading rate of 2 mm $min^{-1}$ with a gauge length of 10 mm. Atomic microscopy (AFM) observation was carried out using a MFP3D microscope (Asylum Research) with a silicon cantilever operating in tapping force mode. SEM images were obtained using a JEOL field-emission scanning electron microscope (JSM-6700F). XPS measurements were performed on a Kratos-Axis spectrometer with monochromatic Al K$\alpha$ (1486.71 eV) X-ray radiation (15 kV and 10 mA) and hemispherical electron energy analyzer. XRD data were recorded with an X-ray diffractometer Bruker AXS D8 using Cu K$\alpha$ radiation (40 kV, 200 mA) with a Ni filter. Electrodeposition, EIS, CV, and chronoamperometric experiments were performed with a CHI 660 D electrochemical workstation (CH Instrument Company). A conventional three-electrode system was adopted. The working electrode was a contacted rGOP with the dimension of 20 mm × 5 mm, and the auxiliary and reference electrodes were Pt foil and Ag/AgCl, respectively. The distance between the electrodes was 0.5 cm in all experiments. For EIS, the frequency range was 0.1 Hz to $10^5$ Hz. Optical microscopy images were obtained using an Olympus71 inverted microscope with an bright-field condenser and colored images were collected using Photometrics CoolSNAP-cf cooled CCD camera.

*Preparation of GOP and rGOP*: The GO was synthesized from synthetic graphite powder based on a modified Hummers method (Supporting Information).[43] Freestanding GOP was fabricated using a simple and scalable mold-casting method. The aqueous dispersion of GO nanosheets was placed in a casting mold made of polytetrafluoroethylene (PTFE). After water was completely evaporated under room temperature, an integral layer of GOP with smooth surfaces could be easily peeled off from the PTFE mold. The size of the as-preapred GOP could be freely adjusted by choosing different sized casting molds, and the thickness of the paper could also be tailored in the range of ≈1 to 30 μm by using different volumes of the GO dispersion. rGOP was prepared by chemical reduction of GOP.[19] In a typical procedure, GOP was directly immersed into an HI solution in a sealed cuvette at room temperature for 1 h. The HI-reduced GOP was washed with deionized (DI) water several times. After being dried at room temperature for 10 h, rGOP was obtained.

*In Situ Electrodeposition $MnO_2$ Nanowires on rGOP*: Typically, $MnO_2$ nanowires were anodically electrodeposited onto the rGOP by immersing the rGOP-contacted working electrode into the 0.1 M $NaSO_4$ containing 50 mM $MnSO_4$ using a CV technique in the potential range from 1.4 V to –1.5 V at the scan rate of 250 mV $s^{-1}$. After electrodeposition, the rGOP were taken out and carefully washed with DI water to remove excessive

electrolyte, dried at 50 °C for 1 h in an oven to remove any residual water. The obtained paper electrode was denoted as $MnO_2$/rGOP. The mass of the $MnO_2$ deposited on the rGOP was determined from the weight difference between the electrode before and after anodic deposition by using a high precision microbalance.

*Ultrasonic-Electrodeposition Pt Nanoparticles on $MnO_2$/rGOP*: Pt nanoparticles were potentiostatic deposition on $MnO_2$/rGOP from a 0.1 M KCl solution containing 1.0 mM $K_2PtCl_6$ by applying a deposition potential of –0.2 V and a deposition time of 150 s. During the deposition process, the electrolyte was under continuous ultrasonic irradiation to minimize the aggregation and reduce the size of the as-obtained nanoparticles. The obtained paper electrode was denoted as Pt–$MnO_2$/rGOP. For comparison, Pt nanoparticles were also deposited on bare rGOP under the same conditions, which was denoted as Pt/rGOP. After electrodeposition, the rGOP were taken out and carefully washed with DI water to remove excessive electrolyte, dried at 50 °C for 1 h in oven to remove any residual water, and then stored in a vacuum desiccator.

*Detection of Extracellular Release of $H_2O_2$*: Human liver cancer HepG2 cells were obtained from ATCC (USA). The cells were maintained in a culture medium consisting of Dulbecco's modified minimum essential medium (37 °C, 5% $CO_2$) and subcultured every 3 days. After centrifuging, the cells were planted at a density of $5 \times 10^4$ cell $mL^{-1}$ in a 24-well microplate. HepG2 cells at a confluency of 80% were used for the electrochemical experiments.

## Supporting Information

Supporting Information is available from the Wiley Online Library or from the author.

## Acknowledgements

H.D. acknowledges the program of Nanyang Assistant Professorship for financial support.

Received: January 20, 2012
Published online: March 21, 2012

[1] M. C. Chuang, Y. L. Yang, T. F. Tseng, T. Chou, S. L. Lou, J. Wang, *Talanta* **2010**, *81*, 15.
[2] W. Y. Wu, X. Zhong, W. Wang, Q. Miao, J. J. Zhu, *Electrochem. Commun.* **2010**, *12*, 1600.
[3] D. Pradhan, F. Niroui, K. T. Leung, *ACS Appl. Mater. Interface* **2010**, *2*, 2409.
[4] C. Li, J. Han, C. H. Ahn, *Biosens. Bioelectron.* **2007**, *22*, 1988.
[5] J. Wang, *J. Pharm. Biomed. Anal.* **1999**, *19*, 47.
[6] R. Cui, C. Liu, J. Shen, D. Gao, J. J. Zhu, H. Y. Chen, *Adv. Funct. Mater.* **2008**, *18*, 2197.
[7] J. Huang, D. Wang, H. Hou, T. You, *Adv. Funct. Mater.* **2008**, *18*, 441.
[8] S. Campuzano, J. Wang, *Electroanalysis* **2011**, *23*, 1289.
[9] P. V. Kamat, *J. Phys. Chem. Lett.* **2010**, *1*, 520.
[10] F. W. Campbell, R. G. Compton, *Anal. Bioanal. Chem.* **2010**, *396*, 241.
[11] H. Chu, Y. Shen, L. Lin, X. Qin, G. Feng, Z. Lin, J. Wang, H. Liu, Y. Li, *Adv. Funct. Mater.* **2010**, *20*, 3747.
[12] R. Lv, T. Cui, M.-S. Jun, Q. Zhang, A. Cao, D. S. Su, Z. Zhang, S.-H. Yoon, J. Miyawaki, I. Mochida, F. Kang, *Adv. Funct. Mater.* **2011**, *21*, 999.
[13] K. S. Novoselov, A. K. Geim, S. V. Morozov, D. Jiang, Y. Zhang, S. V. Dubonos, I. V. Grigorieva, A. A. Firsov, *Science* **2004**, *306*, 666.
[14] S. Stankovich, D. A. Dikin, G. H. B. Dommett, K. M. Kohlhaas, E. J. Zimney, E. A. Stach, R. D. Piner, S. T. Nguyen, R. S. Ruoff, *Nature* **2006**, *442*, 282.
[15] A. K. Geim, K. S. Novoselov, *Nat. Mater.* **2007**, *6*, 183.
[16] D. Li, M. B. Muller, S. Gilje, R. B. Kaner, G. G. Wallace, *Nat. Nanotechnol.* **2008**, *3*, 101.
[17] A. K. Geim, *Science* **2009**, *324*, 1530.
[18] H. Chang, G. Wang, A. Yang, X. Tao, X. Liu, Y. Shen, Z. Zheng, *Adv. Funct. Mater.* **2010**, *20*, 2893.
[19] F. Xiao, J. B. Song, H. C. Gao, X. L. Zan, R. Xu, H. W. Duan, *ACS Nano* **2012**, *6*, 100–110.
[20] D. A. Dikin, S. Stankovich, E. J. Zimney, R. D. Piner, G. H. B. Dommett, G. Evmenenko, S. T. Nguyen, R. S. Ruoff, *Nature* **2007**, *448*, 457.
[21] D. W. Wang, F. Li, J. Zhao, W. Ren, Z. G. Chen, J. Tan, Z. S. Wu, I. Gentle, G. Q. Lu, H. M. Cheng, *ACS Nano* **2009**, *3*, 1745.
[22] S. Pei, J. Zhao, J. Du, W. Ren, H. M. Cheng, *Carbon* **2010**, *48*, 4466.
[23] H. Chen, M. B. Müller, K. J. Gilmore, G. G. Wallace, D. Li, *Adv. Mater.* **2008**, *20*, 3557.
[24] B. G. Choi, H. Park, T. J. Park, M. H. Yang, J. S. Kim, S. Y. Jang, N. S. Heo, S. Y. Lee, J. Kong, W. H. Hong, *ACS Nano* **2010**, *4*, 2910.
[25] R. Kou, Y. Shao, D. Mei, Z. Nie, D. Wang, C. Wang, V. V. Viswanathan, S. Park, I. A. Aksay, Y. Lin, Y. Wang, J. Liu, *J. Am. Chem. Soc.* **2011**, *133*, 2541.
[26] E. Formo, E. Lee, D. Campbell, Y. N. Xia, *Nano Lett.* **2008**, *8*, 668.
[27] S. Y. Huang, P. Ganesan, S. Park, B. N. Popov, *J. Am. Chem. Soc.* **2009**, *131*, 13898.
[28] Z. Y. Zhou, N. Tian, J. T. Li, I. Broadwell, S. G. Sun, *Chem. Soc. Rev.* **2011**, *40*, 4167.
[29] A. Chen, P. Holt-Hindle, *Chem. Rev.* **2010**, *110*, 3767.
[30] F. Xiao, F. Q. Zhao, D. P. Mei, Z. R. Mo, B. Z. Zeng, *Biosens. Bioelectron.* **2009**, *24*, 3481.
[31] F. Xiao, F. Q. Zhao, Y. F. Zhang, G. P. Guo, B. Z. Zeng, *J. Phys. Chem. C* **2009**, *113*, 849.
[32] H. Gao, F. Xiao, C. C. Bun, H. Duan, *ACS Appl. Mater. Interfaces* **2011**, *3*, 3049.
[33] C. M. Welch, C. E. Banks, A. O. Simm, R. G. Compton, *Anal. Bioanal. Chem.* **2005**, *382*, 12.
[34] M. Liu, G. Zhao, K. Zhao, X. Tong, Y. Tang, *Electrochem. Commun.* **2009**, *11*, 1397.
[35] J. S. Long, D. S. Silvester, G. G. Wildgoose, A.-E. Surkus, G.-U. Flechsig, R. G. Compton, *Bioelectrochemistry* **2008**, *74*, 183.
[36] J. Li, L. Liu, F. Xiao, Z. Gui, R. Yan, F. Zhao, L. Hu, B. Zeng, *J. Electroanal. Chem.* **2008**, *613*, 51.
[37] Q. Zeng, J. Cheng, L. Tang, X. Liu, Y. Liu, J. Li, J. Jiang, *Adv. Funct. Mater.* **2010**, *20*, 3366.
[38] W. S. Hummers, R. E. Offeman, *J. Am. Chem. Soc.* **1958**, *80*, 1339.
[39] Y. Shao, J. Wang, M. Engelhard, C. Wang, Y. Lin, *J. Mater. Chem.* **2010**, *20*, 743.
[40] I. F. Cheng, Y. Xie, R. A. Gonzales, P. R. Brejna, J. P. Sundararajan, B. A. F. Kengne, D. E. Aston, D. N. McIlroy, J. D. Foutch, P. R. Griffiths, *Carbon* **2011**, *49*, 2852.
[41] S. Stankovich, D. A. Dikin, R. D. Piner, K. A. Kohlhaas, A. Kleinhammes, Y. Jia, Y. Wu, S. T. Nguyen, R. S. Ruoff, *Carbon* **2007**, *45*, 1558.
[42] H. J. Shin, K. K. Kim, A. Benayad, S. M. Yoon, H. K. Park, I. S. Jung, M. H. Jin, H. K. Jeong, J. M. Kim, J. Y. Choi, Y. H. Lee, *Adv. Funct. Mater.* **2009**, *19*, 1987.
[43] J. Zhang, J. Jiang, X. S. Zhao, *J. Phys. Chem. C* **2011**, *115*, 6448
[44] H. K. Jeong, Y. P. Lee, R. J. Lahaye, M. H. Park, K. H. An, I. J. Kim, C. W. Yang, C. Y. Park, R. S. Ruoff, Y. H. Lee, *J. Am. Chem. Soc.* **2008**, *130*, 1362.
[45] H. L. Guo, X. F. Wang, Q. Y. Qian, F. B. Wang, X. H. Xia, *ACS Nano* **2009**, *3*, 2653.
[46] V. Radmilovic, H. A. Gasteiger, P. N. Ross, *J. Catal.* **1995**, *154*, 98.
[47] Y. Luo, H. Liu, Q. Rui, Y. Tian, *Anal. Chem.* **2009**, *81*, 3035.
[48] Y. Ding, Y. Wang, Y. Lei, *Biosens. Bioelectron.* **2010**, *25*, 2009.
[49] X. Xu, S. Jiang, Z. Hu, S. Liu, *ACS Nano* **2010**, *4*, 4292.
[50] C. X. Guo, X. T. Zheng, S. R. Ng, Y. Lai, Y. Lei, C. M. Li, *Chem. Commun.* **2011**, *47*, 2652.